Journal of Physics: Conference Series **1332** (2019) 012002 doi:10.1088/1742-6596/1332/1/012002

Global Energetics of Solar Flares and Coronal Mass Ejections

Markus J. Aschwanden[1], Amir Caspi[2], Christina M.S. Cohen[3], Gordon Holman[4], Ju Jing[5], Matthieu Kretzschmar[6], Eduard P. Kontar[7], James M. McTiernan[8], Richard A. Mewaldt[3], Aidan O'Flannagain[9], Ian G. Richardson[10], Daniel Ryan[11], Harry P. Warren[12], and Yan Xu[5]

[1] Lockheed Martin, Solar and Astrophysics Laboratory, Org. A021S, Building 252, 3251 Hanover Street, Palo Alto, CA 94304, USA; aschwanden@lmsal.com
[2] Planetary Science Directorate, Southwest Research Institute, Boulder, CO 80302, USA; amir.caspi@swri.org
[3] California Institute of Technology, Mail Code 290-17, Pasadena, CA 91125, USA; rmewaldt@srl.caltech.edu; cohen@srl.caltech.edu
[4] Code 671, NASA Goddard Space Flight Center, Greenbelt, MD 20771, USA; gordon.d.holman@nasa.gov
[5] Institute for Space Weather Sciences, New Jersey Institute of Technology, University Heights, Newark NJ 07102-1982, USA; ju.jing@njit.edu, yan.xu@njit.edu
[6] LPC2E, UMR 6115 CNRS and University of Orléans, 3a Avenue de la recherche scientifique, F-45071 Orléans, France; matthieu.kretzschmar@cnrs-orleans.fr
[7] School of Physics and Astronomy, University of Glasgow, Glasgow G12 8QQ, UK; eduard.kontar@astro.gla.ac.uk
[8] Space Sciences Laboratory, University of California, Berkeley, CA 94720, USA; jimm@ssl.berkeley.edu
[9] Astrophysics Research Group, School of Physics, Trinity College Dublin, Dublin 2, Ireland; aidanoflann@gmail.com
[10] GPHI and Dept. of Astronomy, University of Maryland; Code 672, NASA Goddard Space Flight Center, Greenbelt, MD 20770, USA; ian.g.richardson@nasa.gov
[11] NASA Goddard Space Flight Center, 8800 Greenbelt Road, Greenbelt, MD 20770, USA; ryand5@tcd.ie
[12] Space Science Division, Naval Research Laboratory, Washington, DC 20375, USA; harry.warren@nrl.navy.mil

Abstract. We investigate the global energetics and energy closure of various physical processes that are energetically important in solar flares and coronal mass ejections (CMEs), which includes: magnetic energies, thermal energies, nonthermal energies (particle acceleration), direct and indirect plasma heating processes, kinetic CME energies, gravitational CME energies, aerodynamic drag of CMEs, solar energetic particle events, EUV and soft X-ray radiation, white-light, and bolometric energies. Statistics on these forms of energies is obtained from 400 GOES M- and X-class events during the first 3.5 years of the Solar Dynamics Observatory (SDO) mission. A

primary test addressed in this study is the closure of the various energies, such as the equivalence of the dissipated magnetic energies and the primary dissipated flare energies (accelerated particles, direct heating, CME acceleration), which faciliate the energy of secondary processes (plasma heating, shock acceleration) and interactions with the solar wind (aerodynamic drag). Our study demonstrates energy closure in the statistical average, while individual events may have considerable uncertainties, requiring improved nonlinear force-free field models, and particle acceleration models with observationally constrained low-energy cutoffs.

1. THEORETICAL CONCEPTS

The energy flow in solar flares and coronal mass ejections (CMEs) passes through several processes, which are depicted in the diagram of Fig. 1. Initially, a stable nonflaring active region exists with a near-potential magnetic field with energy E_p, which then becomes twisted and sheared, building up nonpotential energy E_{np} and the free energy, $E_{free} = E_{np} - E_p$, of which a fraction $E_{mag} \leq E_{free}$ is dissipated during a flare (e.g., [1, 2]). There are three primary energy dissipation processes that follow after a magnetic instability, typically a magnetic reconnection process, spawning (i) the acceleration of nonthermal particles (e.g., reviews by [3–7], with electron energy $E_{nt,e}$ and ion energy $E_{nt,i}$, providing (ii) direct heating in the magnetic reconnection region, E_{dir} (e.g., [8–10]); these are often accompanied by (iii) an eruptive process, which can be a complete eruption of a CME or filament, or a semi-eruptive energy release, also known as "failed eruption", in the case of a confined flare (e.g., Török and Kliem [11]). The CME process carries an energy of $E_{cme} = E_{kin} + E_{grav}$, consisting of the kinetic energy E_{kin} and the gravitational potential energy E_{grav}, to lift a CME from the solar surface into the heliosphere. These primary energy dissipation processes allow us to test the primary energy closure equation,

$$E_{mag} = E_{nt} + E_{dir} + E_{cme} = (E_{nt,e} + E_{nt,i}) + E_{dir} + (E_{cme}^{kin} + E_{cme}^{grav} - E_{drag}) \ , \quad (1)$$

where the left side of the equation contains the total (magnetic) energy input (or storage) and the right side contains the total energy output (or dissipation). There is additional energy supply by the aerodynamic drag E_{drag}, which appears as a negative quantity on the right-hand side of Eq. (1) because it is supplied by the slow solar wind and reduces the magnetic energy demand in the flare region. After this primary step in the initiation of a flare and CME, secondary energy dissipation processes kick in. Nonthermal particles are accelerated along bi-directional trajectories that lead out of the magnetic reconnection region, where most particles precipitate down to the chromosphere, then heat the chromospheric plasma and drive evaporation of the heated plasma up into the corona (e.g., Antonucci and Dennis [12]), while other particles escape into interplanetary space (see reviews by [13–15]). The flare arcade that becomes filled with heated chromospheric plasma, radiates, and looses its energy by conduction and radiation in soft X-rays (SXR) and extreme ultraviolet (EUV). The thermal energy content E_{th} can be calculated from the total emission measure observed in SXR and EUV and should not exceed the nonthermal energy, $E_{nt} = E_{nt,e} + E_{nt,i}$, unless there are other heating processes besides the electron beam-driven heating observed in hard

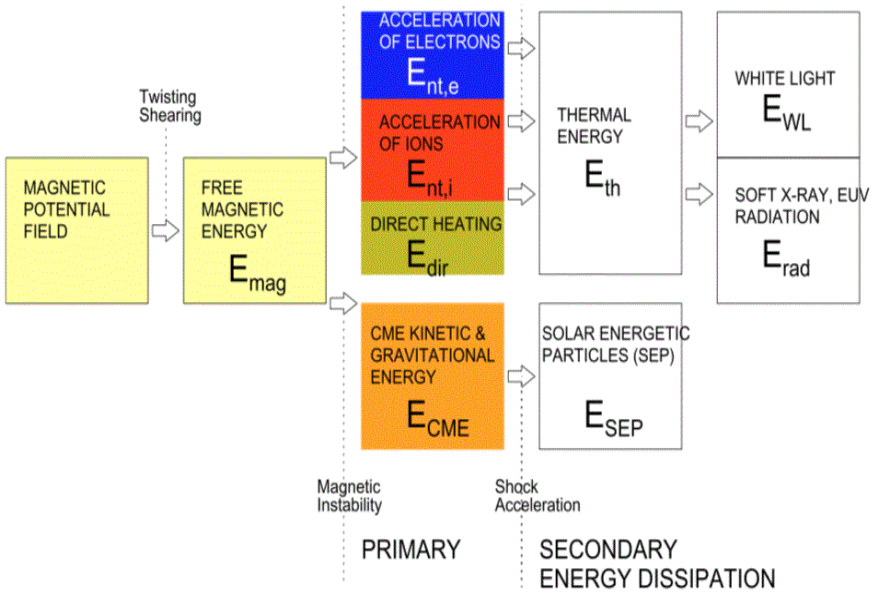

Figure 1. Schematic diagram of energy input (free magnetic energy E_{mag}), primary energy dissipation processes (electron acceleration $E_{nt,e}$, ion acceleration $E_{nt,i}$, direct heating E_{dir}, and launching of CME (E_{cme}), and secondary energy dissipation processes (thermal energy E_{th}, solar energetic particles E_{sep}, bolometric luminosity, and radiative energies observed in white light E_{WL}, soft X-rays, and EUV E_{rad} (Aschwanden et al [27]).

X-rays (according to the thick-target bremsstrahlung model of Brown 1971). Thus we can test the following energy inequality between thermal and nonthermal energies (if we neglect direct heating),

$$E_{th} \leq E_{nt} = E_{nt,e} + E_{nt,i} \ . \tag{2}$$

Radiation is produced not only at SXR and EUV wavelengths (E_{th}), but also in visible and near-ultraviolet wavelengths, recorded as white-light flare emission; this is the largest contributor to the bolometric energy or luminosity E_{bol}, which contains vastly more radiative energy than observed in SXR [16–18]. Using a superimposed epoch analysis of 2100 C, M, and X-class flares, Kretzschmar et al [19] and Kretzschmar ([18] and Table 1 therein) calculated the total solar irradiance for five synthesized flare time profiles. The continuum emission produced by white-light flares determined in this way allows us to compare another pair of energies – the total thermal energy E_{th} and the bolometric luminosity, produced by the flare impact of precipitating particles, radiative backwarming, and locally enhanced ionization, enhancing bound—free and free—continuum emission (e.g., [20–25]),

$$E_{bol} \approx E_{th} \ . \tag{3}$$

Another secondary process is the acceleration of nonthermal particles by the CME, which is produced by shock acceleration in very fast CMEs, observed in the form of *solar*

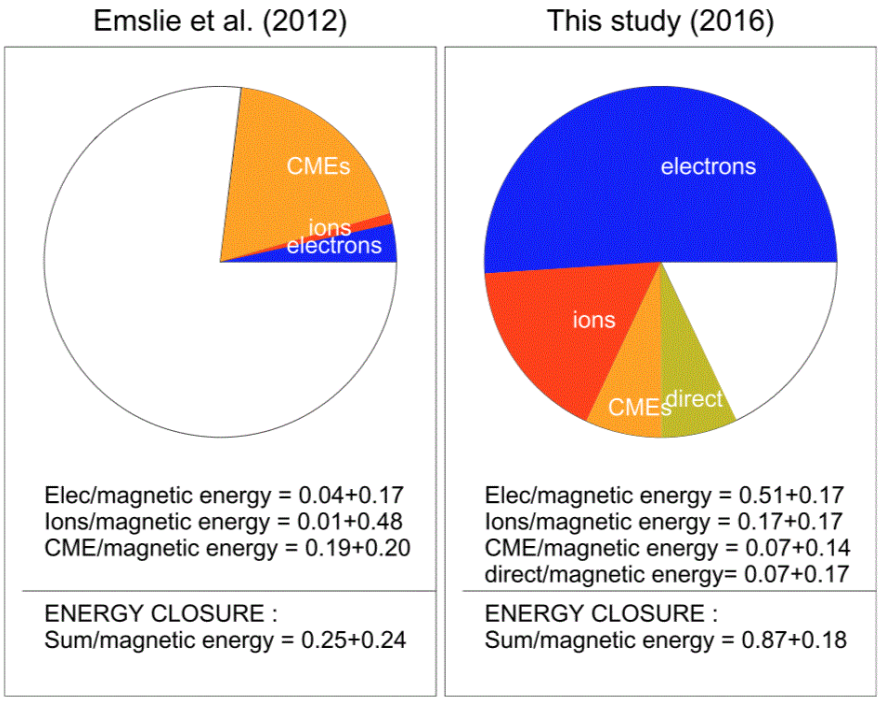

Figure 2. Pie chart of energy closure, obtained from previous work of Emslie et al [28] (left panel) and from the study of Aschwanden et al [27]. The full area of each pie chart is normalized to the total dissipated magnetic energies in flares. Testing the closure of energies, there is a discrepancy of over-estimating the magnetic energy by a factor of 4 in [28], which is reduced to a factor of 1.15 in the study of [27].

energetic particle (SEP) events (e.g., see review by Reames 2013 [26]), which allows us to test another energy inequality,

$$E_{sep} \leq E_{cme} = E_{kin}^{cme} + E_{grav}^{cme} \ . \tag{4}$$

The energy closure studied here depends, of course, on specific physical models of flares and CMEs. In this discussion we should be aware of the caveat that alternative flare models may deviate from the energy closure relationships and the inequalities discussed here. Another important issue in any energy closure relationship concerns the double-counting of energies if there are multiple energy conversion processes acting at the same time or nearly simultaneously. We attempt to distinguish between primary and secondary energy dissipation mechanisms, as shown in Figure 1.

2. OBSERVATIONAL RESULTS

2.1. Magnetic Energies

We measured the magnetic field in a large number (in about 200 cases out of the 400 flaring active regions) (Aschwanden et al [2]) by using the *vertical-current approximation nonlinear force-free field code (VCA-NLFFF)* [29, 30]. This deduces the

magnetic potential field $\mathbf{B}_p$ from photospheric magnetograms $B_z(x, y)$ observed with the *Helioseismic and Magnetic Imager (HMI)* onboard the *Solar Dynamic Observatory (SDO)*, and measures the non-potential field $\mathbf{B}_{np}$ by forward-fitting of nonpotential field lines to coronal loop structures observed in EUV with the *Atmospheric Imager Assembly (AIA)* onboard SDO, which are automatically traced with the *Oriented Coronal Curved Loop Tracing (OCCULT)* code (Aschwanden et al [31]). The obtained magnetic parameters exhibit scaling laws for the nonpotential energy, $E_{np} \propto E_p^{1.02}$, for the free energy, $E_{free} \propto E_p^{1.7}$ and $E_{free} \propto B_\varphi^{1.0} L^{1.5}$ (where B_φ is the azimuthally twisted field component), for the dissipated energy, $E_{diss} \propto E_p^{1.6}$ and $E_{diss} \propto E_{free}^{0.9}$, and the energy dissipation volume, $V \propto E^{1.2}$. The potential energies vary in the range of $E_p = 1 \times 10^{31}$ — 4×10^{33} erg, while the free energy has a ratio of $E_{free}/E_p \approx 1\%$ — 25%. The Poynting flux amounts to $F_{flare} \approx 5 \times 10^8 - 10^{10}$ erg cm^{-2} s^{-1} during flares, which averages to $F_{AR} \approx 6 \times 10^6$ erg cm^{-2} s^{-1} during the entire observation period, and is comparable with the coronal heating rate requirement in active regions. Caveats of the calculation of magnetic energies includes the accuracy of non-potential energies obtained from the vertical-current approximation, and the detectability of the step-wise decrease of the free energy during the flare duration. It appears that a coronal illumination effect (e.g., chromospheric evaporation) is necessary to detect the full free energy in the preflare phase.

2.2. Thermal Energies

The thermal energies of the same data set of $\approx$ 400 M and X-class flares have been inferred from the multi-wavelength images observed with the *Atmospheric Imaging Assembly (AIA)* onboard the SDO (Aschwanden et al [32]). We compute the *differential emission measure (DEM)* distribution functions and associated multi-thermal energies, using a spatially-synthesized Gaussian DEM forward-fitting method. The multi-thermal DEM function yields a significantly higher energy (by an average factor of $\approx$ 14) than an isothermal energy estimate at the peak of the DEM. We find a statistical energy ratio of $E_{th}/E_{diss} \approx 2\%$ — 40% between the multi-thermal energy E_{th} and the magnetically dissipated energy E_{diss}, which is an order of magnitude higher than the estimates of Emslie et al [28]. For the analyzed set of M and X-class flares we find the following physical parameter ranges: $L = 10^{8.2} - 10^{9.7}$ cm for the length scale of the flare areas, $T_p = 10^{5.7} - 10^{7.4}$ K for the DEM peak temperature, $T_w = 10^{6.8} - 10^{7.6}$ K for the emission measure-weighted temperature, $n_p = 10^{10.3} - 10^{11.8}$ cm^{-3} for the average electron density, $EM_p = 10^{47.3}$–$10^{50.3}$ cm^{-3} for the DEM peak emission measure, and $E_{th} = 10^{26.8} - 10^{32.0}$ erg for the multi-thermal energies. The deduced multi-thermal energies are consistent with the *Rosner-Tucker-Vaiana 1978 (RTV)* [33] scaling law, $E_{th,RTV} = 7.3 \times 10^{-10} T_p^3 L_p^2$, which predicts extremal values of $E_{th,max} \approx 1.5 \times 10^{33}$ erg for the largest flare, and $E_{th,min} \approx 1 \times 10^{24}$ erg for the smallest coronal nanoflare. The size distributions of the spatial parameters exhibit powerlaw tails that are consistent with the predictions of the fractal-diffusive self-organized criticality model, combined with the RTV scaling law (Aschwanden 2012 [14]). Note that the thermal energies quantify a secondary energy dissipation process (in the thick-target model of Brown 1971), produced after the primary magnetic energy dissipation by accelerated electrons, ions, and direct plasma heating in the magnetic reconnection region. Nevertheless, the multi-thermal energies can be

used as an upper limit for the precipitating electron flux that spawns chromospheric evaporation (Eq. 2).

2.3. Non-Thermal Energies

Using the *Ramaty High-Energy Solar Spectroscopic Imager (RHESSI)* data of 191 M and X-class flare events from the same data set discussed before, we fit a thermal and a nonthermal component to RHESSI spectra, which yields the temperature of the differential emission measure (DEM) tail, the nonthermal power law slope and flux, and the thermal/nonthermal cross-over energy e_{co}. From these parameters we calculate the total nonthermal energy E_{nt} in electrons with two different methods: (i) using the observed cross-over energy e_{co} as low-energy cutoff, and (ii) using the low-energy cutoff e_{wt} predicted by the warm thick-target bremsstrahlung model of Kontar et al [35]. Based on a mean temperature of $T_e = 8.6$ MK in active regions we find low-energy cutoff energies of $e_{wt} = 6.2 \pm 1.6$ keV for the warm-target model, which is significantly lower than the cross-over energies $e_{co} = 21 \pm 6$ keV. Comparing with the statistics of magnetically dissipated energies E_{mag} and thermal energies E_{th} from the two previous studies, we find the following mean (logarithmic) energy ratios with the warm-target model: $E_{nt} = 0.41E_{mag}$, $E_{th} = 0.08E_{mag}$, and $E_{th} = 0.15E_{nt}$. The total dissipated magnetic energy exceeds the thermal energy in 95% and the nonthermal energy in 71% of the flare events, which confirms that magnetic reconnection processes are sufficient to explain flare energies. The nonthermal energy exceeds the thermal energy in 85% of the events, which largely confirms the warm thick-target model. In future work we may use the number of accelerated electrons in the flare volume (as estimated from the measured flare area and vertical scale height) as an independent additional constraint for the low-energy cutoff of the nonthermal electron injection spectrum.

2.4. CME Energies

We determine the mass m_{cme}, the kinetic energy E_{kin}, and the gravitational potential energy E_{grav} of CMEs in the same AIA/SDO dataset of 400 M and X-class flare events mentioned before, using a new method based on the EUV dimming effect [36]. EUV dimming is modeled in terms of a 3-D geometric volume that encompasses a CME footprint area in the lower corona and expands adiabatically into the upper corona and heliosphere. Such a dynamic CME model is fitted to the observed evolution of the total emission measure observed in EUV. The model derives the evolution of the CME volume $V(t)$, the mean electron density $n_e(t)$, the emission measure $EM(t)$, the bulk plasma expansion velocity $v(t)$, the mass m_{cme} (being constant in time), and the kinetic energy $E_{kin}(t)$ in the CME source region. The EUV dimming method is truly complementary to the Thomson scattering method in white light, which probes the CME evolution in the heliosphere at distances of $r \gtrsim 2R_{\odot}$, while the EUV dimming method tracks the CME launch in the corona. CME energies are found to be systematically lower than the dissipated magnetic energies, which is consistent with a magnetic origin of CMEs.

We refine the CME model and apply it to (860) GOES M- and X-class flare events observed during the first seven years (2010—2016) of the SDO mission [37]. The model refinements include: the 3-D geometry of CMEs, the gravitational deceleration, the relationship between the center-of-mass motion and the leading-edge motion observed

in white-light coronagraphs, and the application of the Rosner—Tucker—Vaiana scaling law. The refined CME model based on EUV-dimming observed in AIA/SDO data complements the traditional white-light scattering model, using the Large-Angle and Spectrometric Coronagraph Experiment (LASCO) onboard the *Solar and Heliospheric Observatory*. The CME masses, speeds, and kinetic energies determined from both AIA and LASCO are found to agree on average. Empirical scaling laws were found, i.e., $v \propto T_e^{1/2}$, $v \propto (m_{cme})^{1/4}$, and $m_{cme} \propto L^2$, which indicate scaling laws for CME parameters.

The most recent work on CME energetics includes the aerodynamic drag force, which represents an external energy source that accelerates low—speed CME's to the slow solar wind speed of $w \approx 400$ km, and slows down initially fast CMEs to the slow solar wind speed. Preliminary estimates indicate that the CME energy budget reduces from 7% of the total dissipated magnetic energy to $\approx 5\%$, thanks to the acceleration conveyed by the aerodynamic drag. Moreover, the aerodynamic drag model [38, 39] predicts arrival times of CMEs at Earth with an accuracy of $\approx 23\%$ [40].

2.5. Solar Energetic Particles (SEPs)

SEP energies were calculated from observations by the STEREO A and B spacecraft and near-Earth spacecraft. Since most flares are not associated with SEP events, and many SEP events overlap with, and are difficult to separate from other events, estimates of SEP energies were only made for a small number of the 400 M and X-class flares in [27]. Estimates for 10 SEP events observed at both STEREO spacecraft and the Earth are given in Table 1 of [27], where further details of the analysis are also available. These events give a ratio $E_{sep}/E_{cme} = 0.03 \pm 0.45$, comparable with the [28] result of ≈ 0.04. The low ratio is consistent with our notion of CME-driven acceleration leading to SEP events being a secondary energy conversion process The ratio of the magnetic and SEP energies is only available for four events, which give $E_{sep}/E_{mag} = 0.1 \pm 1.64$. Notwithstanding the large error, the low ratio confirms that the magnetic free energy in the flare region is sufficient to explain the energetics of SEP particles, regardless of whether they are accelerated in the coronal flare region or in interplanetary shocks.

3. CONCLUSIONS

The results of the energy budget or energy partition of different forms of energies during a solar flare/CME event is summarized in Fig. 2. In the pioneering work of Emslie et al [28], the major constituents are accelerated electrons ($4\% \pm 17\%$), accelerated ions ($1\% \pm 48\%$), and CME kinetic energies in the slow solar wind frame ($19\% \pm 20\%$), which add up to $25\% \pm 24\%$ of the dissipated magnetic energy. The lack of closure is most likely caused by the (ad hoc) four-fold over-estimate of the magnetic free energy. A series of recent studies dedicated to the global energetics of flares and CMEs finds the following overall average ratios of $51\% \pm 17\%$ for electron acceleration, $17\% \pm 17\%$ for ion acceleration, $7\% \pm 14\%$ for CME kinetic energies, and $7\% \pm 17\%$ for direct heating, which add up to closure ($87\% \pm 18\%$) [2, 32, 41, 27, 40, 36]. *Solar energetic particle (SEP)* events draw a relatively small fraction of a few percent from the energy of a CME shock front. The largest uncertainties, mostly due to a lack of suitable energy and magnetic field models, are attributed to the measurement of changes in the free (magnetic) energy,

direct heating during flares, the low-energy cutoff of nonthermal particles, CME halo geometries, and bolometric flare luminosities.

We acknowledge useful discussions with John Raymond, Nat Gopalswamy, Edmond Roelof, Richard Mewaldt, HaiHoing Che, and other participants of the 18^{th} meeting on Energetic Particles in Pasadena, February 2019. This work was partially supported by NASA contracts NNX11A099G, NNG04EA00C (SDO/AIA), and NNG09FA40C (IRIS).

References

[1] Schrijver, C.J., DeRosa, M.L., Metcalf, T., 2008, *ApJ* 675, 1637
[2] Aschwanden, M.J., Xu, Y., Jing, J., 2014, *ApJ* 797, 50
[3] Miller, J.A., Cargill, P.J., Emslie, A.G., 1997, *JGR* 102/A7, 14631
[4] Aschwanden, M.J., 2002, *Space Science Reviews* 101, 1
[5] Aschwanden, M.J.. 2004, *Physics of the Solar Corona. An Introduction*, Berlin: Springer and Praxis, p.216
[6] Benz, A.O., 2008, *Living Reviews in Solar Physics* 5, 1
[7] Holman, G.D., Aschwanden, M.J., Aurass, H., 2011, *Space Sci Rev* 159, 107
[8] Sui, L. and Holman, G.D., 2003, *ApJL* 596, L251
[9] Caspi, A. and Lin, R.P. 2010, *ApJ* 725, L161
[10] Caspi, A., Shih, A.Y., McTiernan, J.M., and Krucker, S. 2015, *ApJ* 811, L1
[11] Török, T. and Kliem, B. 2005, *ApJ* 630, L97
[12] Antonucci, E. and Dennis, B.R. 1983, *Solar Phys.* 86, 67
[13] Hudson, H.S. and Ryan, J. 1995, *ARAA* 33, 239
[14] Aschwanden, M.J. 2012, *A&A* 539, A2.
[15] Lin, R.P. 2007, *Space Sci Rev* 124, 233
[16] Woods, T.N., Eparvier, F.G., Fontenla, J., et al. 2004, *GRL* 31, L10802
[17] Woods, T.N., Kopp, G., and Chamberlin, P.C. 2006, *JGR (Space Physics)*, 111, 10
[18] Kretzschmar, M. 2011, *A&A*, 530, A84
[19] Kretzschmar, M., Dudok de Wit, T., Schmutz, W., et al. 2010, *Nature Physics*, 6(9), 690
[20] Najita, K. and Orrall, F.Q. 1970, *Solar Phys*, 15, 17
[21] Hudson, H.S. 1972, *Solar Phys*, 24, 414
[22] Ding, M.D., Liu, Y., Yeh, C.-T., and Li, J.P. 2003, *A&A*, 403, 1151
[23] Battaglia, M. and Kontar, E.P. 2011, *ApJ*, 735, 42
[24] Battaglia, M., Kontar, E.P., and Hannah,I.G. 2011, *A&A* 526, A3
[25] Xu,Y., Jing, J., Wang, S., and Wang, H. 2014, *ApJ*, 787, 7
[26] Reames, D.V. 2013, *Space Science Reviews*, 175, 53
[27] Aschwanden, M.J., Caspi, A., Cohen, C.M.S., et al. 2017, *ApJ*, 836, 17
[28] Emslie, A.G., Dennis, B.R., Shih, A. Y., et al. 2012, *ApJ*, 759, 71
[29] Aschwanden, M.J. 2013, *Solar Phys.*, 287, 323
[30] Aschwanden, M.J. 2016b, *ApJSS* 224, 25
[31] Aschwanden, M.J., DePontieu, B., and Katrukha, E. 2013, Entropy, 15(8), 3007
[32] Aschwanden, M.J., Boerner, P., Ryan, D., et al. 2015, *ApJ* 802, 53
[33] Rosner, R., Tucker, W.H., and Vaiana, G.S. 1978, *ApJ*, 220, 643
[34] Brown, J.C. 1971, *Solar Phys.* 18, 489
[35] Kontar, E.P., Jeffrey, N.L.S., Emslie, A.G., and Bian, N.H. 2015, *ApJ* 809, 35
[36] Aschwanden, M.J. 2016a, *ApJ* 831, 105
[37] Aschwanden, M.J. 2017, ApJ 847, 27
[38] Cargill, P.J. 2004, *Solar Phys.*, 221, 135
[39] Vrsnak, B., Zic, T., Vrbanec, D., et al. 2013, *Solar Phys.*, 285, 295
[40] Aschwanden, M.J. 2019, *New Millennium Solar Physics*, Section 11.8, New York: Springer, (in press), http://www.lmsal.com/∼aschwand/bookmarks_books2.html.
[41] Aschwanden, M.J., Holman, G., O'Flannagain, A., et al. 2016, ApJ 832, 27.